Title

Beyond triplet: Unconventional superconductivity in a spin-3/2 topological semimetal

Permalink
https://escholarship.org/uc/item/6r34j85g

Journal
Science Advances, 4(4)

ISSN
2375-2548

Authors
Kim, Hyunsoo
Wang, Kefeng
Nakajima, Yasuyuki
et al.

Publication Date
2018-04-06

DOI
10.1126/sciadv.aao4513

Peer reviewed

CONDENSED MATTER PHYSICS

Beyond triplet: Unconventional superconductivity in a spin-3/2 topological semimetal

Hyunsoo Kim,[1,2,3]* Kefeng Wang,[1,2] Yasuyuki Nakajima,[1,2,4] Rongwei Hu,[1,2] Steven Ziemak,[1,2] Paul Syers,[1,2] Limin Wang,[1,2] Halyna Hodovanets,[1,2] Jonathan D. Denlinger,[5] Philip M. R. Brydon,[6,7] Daniel F. Agterberg,[8] Makariy A. Tanatar,[3] Ruslan Prozorov,[3] Johnpierre Paglione[1,2]*

In all known fermionic superfluids, Cooper pairs are composed of spin-1/2 quasi-particles that pair to form either spin-singlet or spin-triplet bound states. The "spin" of a Bloch electron, however, is fixed by the symmetries of the crystal and the atomic orbitals from which it is derived and, in some cases, can behave as if it were a spin-3/2 particle. The superconducting state of such a system allows pairing beyond spin-triplet, with higher spin quasi-particles combining to form quintet or septet pairs. We report evidence of unconventional superconductivity emerging from a spin-3/2 quasi-particle electronic structure in the half-Heusler semimetal YPtBi, a low-carrier density noncentrosymmetric cubic material with a high symmetry that preserves the *p*-like $j = 3/2$ manifold in the Bi-based Γ_8 band in the presence of strong spin-orbit coupling. With a striking linear temperature dependence of the London penetration depth, the existence of line nodes in the superconducting order parameter Δ is directly explained by a mixed-parity Cooper pairing model with high total angular momentum, consistent with a high-spin fermionic superfluid state. We propose a $\mathbf{k} \cdot \mathbf{p}$ model of the $j = 3/2$ fermions to explain how a dominant $J = 3$ septet pairing state is the simplest solution that naturally produces nodes in the mixed even-odd parity gap. Together with the underlying topologically nontrivial band structure, the unconventional pairing in this system represents a truly novel form of superfluidity that has strong potential for leading the development of a new series of topological superconductors.

INTRODUCTION

When spin-orbit coupling (SOC) is strong enough to rearrange the order of electronic energy bands, various topological phases arise, and the interplay between superconductivity and the topologically ordered phase is of particular interest. The noncentrosymmetric half-Heusler compounds containing heavy metallic elements exhibit strong SOC, which can invert the Bi-derived *s*-like Γ_6 and *p*-like Γ_8 bands, giving a semimetal system with nontrivial topological electronic structure (*1*–*3*). The observation of superconductivity in the RTBi (where R = rare earth and T = Pt or Pd) (*4*, *5*) has added a new richness to these materials that compounds topological aspects of normal-state band structure, superconductivity, and even magnetic order (*6*). In the superconducting state wave function, nontrivial topologies can arise both in fully gapped superconductors (*7*) and unconventional superconductors with point or line nodes, particularly in Weyl and noncentrosymmetric superconductors (*8*). In the latter, the lack of parity symmetry can lead to mixed even-odd parity pairing states on spin-split Fermi surfaces due to antisymmetric SOC (ASOC) (*9*).

The situation in these materials is further enriched by the $j = 3/2$ total angular momentum index of the states in the Γ_8 electronic band near the chemical potential. This arises from the strong atomic SOC of the $s = 1/2$ spin and the $l = 1$ orbital angular momenta in the *p* atomic states of Bi. The high crystal symmetry and the relatively simple band structure conspire to preserve the $j = 3/2$ character of the low-energy electronic states, permitting Cooper pairs with angular momentum beyond the usual spin-singlet or spin-triplet states. In particular, as demonstrated schematically in Fig. 1, high–angular momentum pairing components with quintet ($J = 2$) and septet ($J = 3$) states are possible through the pairing combinations of spin-1/2 and spin-3/2 quasi-particles, giving rise to the possibility of the high-spin superfluidity (*10*–*12*). Such an unprecedented exotic pairing state arises from new $j = 3/2$ interactions that do not appear for the spin-1/2 case, allowing new opportunities for topological superconducting states (*13*).

Here, we focus on the archetype topological half-Heusler YPtBi, a clean limit superconductor with an extremely small electronic density of states at the Fermi level (*4*, *14*), corresponding to a tiny carrier density $n \approx 2 \times 10^{18}$ cm^{-3} (*4*) that rivals that of the record holder SrTiO$_3$ (*15*). The superconducting phase transition at $T_c \approx 0.8$ K (*4*) cannot be explained within the Bardeen-Cooper-Schrieffer (BCS) theory framework, which would require a carrier density nearly three orders of magnitude larger to explain the superconducting phase temperature (*16*), and the upper critical field $H_{c2}(0) = 1.5$ T exceeds the orbital pair-breaking limit for a conventional *s*-wave pairing state (*4*, *17*). The linear temperature dependence of the upper critical field over the entire superconducting temperature range (*4*, *17*) resembles that seen in the topological superconductors, such as Cu$_x$Bi$_2$Se$_3$ (*18*) and Bi$_2$Se$_3$ under pressure (*19*).

RESULTS

To establish a proper pairing model for YPtBi, understanding the electronic structure is essential. Generally, the crystal electric field in a face-centered cubic crystal structure splits the degenerate atomic energy levels into twofold degenerate conduction band and two- and fourfold degenerate valence bands at the Γ-point as shown in Fig. 2A (left). As the atomic SOC of Bi becomes stronger, the valence bands push each other. In YPtBi, the SOC is sufficiently strong to invert the order of the bands, pushing the *p*-like Γ_8 band above the *s*-orbital–derived Γ_6 band.

---

[1]Center for Nanophysics and Advanced Materials, University of Maryland, College Park, MD 20742, USA. [2]Department of Physics, University of Maryland, College Park, MD 20742, USA. [3]Ames Laboratory, Department of Physics and Astronomy, Iowa State University, Ames, IA 50011, USA. [4]Department of Physics, University of Central Florida, Orlando, FL 32816, USA. [5]Advanced Light Source, Lawrence Berkeley National Laboratory, Berkeley, CA 94720, USA. [6]Condensed Matter Theory Center and Joint Quantum Institute, Department of Physics, University of Maryland, College Park, MD 20742, USA. [7]Department of Physics, University of Otago, P.O. Box 56, Dunedin 9054, New Zealand. [8]Department of Physics, University of Wisconsin, Milwaukee, WI 53201, USA.
*Corresponding author. Email: hyunsoo@umd.edu (H.K.); paglione@umd.edu (J.P.)

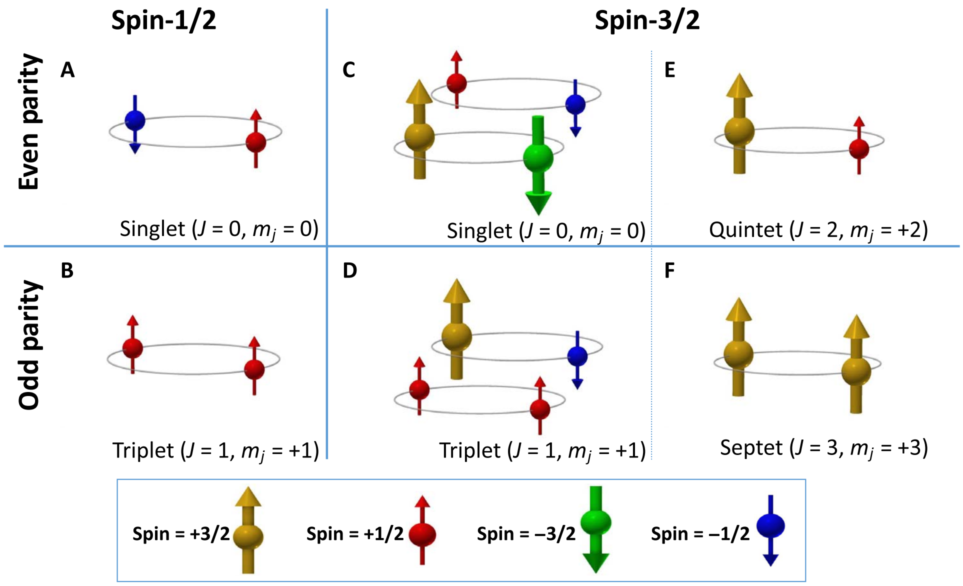

Fig. 1. High-spin Cooper pairing. In conventional spin 1/2 systems, there exists four pairing channels among the spin −1/2 and 1/2 states: one spin-singlet state (with total angular momentum given by $J = 0$ and with the z component of angular momentum, J_z, given by $m_J = 0$) and three spin-triplet states, with $J = 1$ and $m_J = -1$, 0, and 1. The Pauli exclusion principle requires the antisymmetric even-valued J states to have even spatial parity and the symmetric odd-valued J states to have odd spatial parity. The spin-singlet $J = 0$, $m_J = 0$ Cooper pair is depicted in (**A**), whereas the spin-triplet $J = 1$, $m_J = 1$ Cooper pair is depicted in (**B**). For the spin 3/2 systems, there exist 16 pairing channels among the spin −3/2, −1/2, 1/2, and 3/2 states: one spin-singlet state with $J = 0$ and $m_J = 0$; three spin-triplet states with $J = 1$ and $m_J = -1$, 0, and 1; five spin-quintet states with $J = 2$ and $m_J = -2$, −1, 0, 1, and 2; and seven spin-septet states with $J = 3$ and $m_J = -3$, −2, −1, 0, 1, 2, and 3 (see the Supplementary Materials for complete listing). The highest m_J state for each J is depicted in (**C**) to (**F**). In (C), the $J = 0$, $m_J = 0$ spin-singlet pair is a quantum superposition of two Cooper pairs, with one pair made from spins −1/2 and 1/2 and the other pair made from spins −3/2 and 3/2. In (D), the $J = 1$, $m_J = 1$ spin-triplet pair is a quantum superposition of two Cooper pairs, with one made from two paired spin 1/2 states and the other from pairing spin 3/2 with spin −1/2. (E) and (F) show the $J = 2$, $m_J = 2$ and $J = 3$, $m_J = 3$ states, respectively.

This produces a topological semimetal where the low-energy states have spin-3/2 character.

To characterize the band structure in YPtBi, we use density functional theory (DFT) calculations. The calculated bands near the Fermi level along the high symmetry points are shown in Fig. 2B, confirming the topological band inversion of *s*-like Γ_6 and *p*-like Γ_8 bands as shown previously (*20*, *21*). Lacking inversion symmetry splits the spin-degenerate band (*22*). A maximum spin splitting near the chemical potential is observed along [111] (Γ-L) and zero-splitting degeneracy along [100] (Γ-X). The theoretical chemical potential lies on the band touching point. However, experimental chemical potentials are located at −35 and −300 meV determined by quantum oscillation (*4*) and angle-resolved photoemission spectroscopy (ARPES) (*23*, *24*) experiments, respectively (see the Supplementary Materials for details).

The most interesting aspect of the band inversion and the position of the experimental chemical potential in the Γ_8 band arise due to the $j = 3/2$ total angular momentum, which comes from the SOC of spin $s = 1/2$ electrons in the $l = 1$ p orbitals of Bi. Near the Fermi energy, we model the Γ_8 bands by a $j = 3/2$ $\mathbf{k}\cdot\mathbf{p}$ theory (*25*). Up to quadratic order in k, the single-particle Hamiltonian is

$$H = \alpha k^2 + \beta\sum_i k_i^2 \check{J}_i^2 + \gamma\sum_{i\neq j} k_i k_j \check{J}_i \check{J}_j + \delta\sum_i k_i(\check{J}_{i+1}\check{J}_i\check{J}_{i+1} - \check{J}_{i+2}\check{J}_i\check{J}_{i+2}) \qquad (1)$$

where $i = x$, y, and z and $i + 1 = y$ if $i = x$, etc., and $\check{J}_i$ are 4×4 matrix representations of the $j = 3/2$ angular momentum operators. The first line of Eq. 1 is the Luttinger-Kohn model, whereas the second line is the ASOC due to the broken inversion symmetry in YPtBi. The parameters α, β, γ, and δ are chosen by fitting to our ab initio calculations adjusted against ARPES results by matching the bulk bands Γ_6 and Γ_7 (see fig. S1 for details), which yield $\alpha = 20.5$ eVa^2/π^2, $\beta = -18.5$ eVa^2/π^2, $\gamma = -12.7$ eVa^2/π^2, and $\delta = 0.06$ eVa/π by fixing the chemical potential at $u = -35$ meV, estimated by using quantum oscillation frequency $F = 46$ T with a parabolic band (see the Supplementary Materials for details). Here, a is the lattice constant taken from the study by Haase *et al.* (*26*). The observed low density of hole carriers is consistent with a Fermi energy lying close to the top of the hole bands, yielding typical Fermi surfaces shown in Fig. 2C.

The Hamiltonian Eq. 1 has two major implications for the superconductivity in YPtBi. First, because the quasi-particles in the Γ_8 band have intrinsic angular momentum $j = 3/2$, they can form Cooper pairs with higher intrinsic angular momentum than allowed in the conventional theory of $j = 1/2$ quasi-particle pairing; specifically, in addition to the familiar singlet ($J = 0$) and triplet ($J = 1$) states, we must also consider quintet ($J = 2$) and septet ($J = 3$) pairing (see the Supplementary Materials for full set of states). Second, the absence of inversion symmetry (manifested by ASOC) implies that a stable superconducting state will be dominated by pairing between quasi-particles in time-reversed states near the Fermi energy (*9*). As detailed in the Supplementary Materials, this condition is generically satisfied by a mixture of conventional *s*-wave singlet pairing with an unconventional *p*-wave septet pairing state (*13*). We emphasize that this unconventional superconducting state cannot occur for Cooper pairs made from pairing usual $j = 1/2$ states. The proposed superconducting states do not depend on the details of the band structure, for example, local density approximation (LDA) or modified Becke–Johnson LDA (MBJLDA). The key

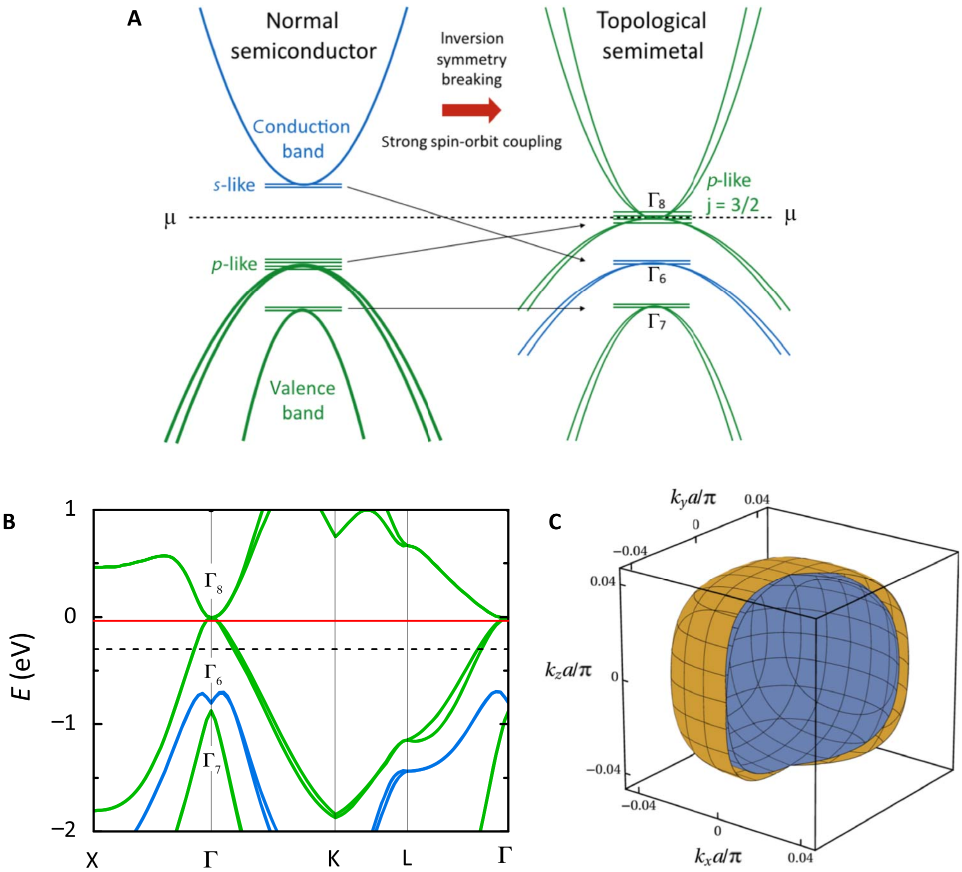

Fig. 2. Topological band structure and spin-split Fermi surface of YPtBi. The effect of strong SOC on a normal semiconductor band structure acts to produce a topological semimetal, which retains the spin-3/2 character of the original p-like band. As shown schematically in (**A**), as SOC is increased, the s-like conduction band is pushed below the chemical potential μ, whereas the fourfold-degenerate p-like valence band at the Γ-point is pushed up to the chemical potential forming spin j = 3/2 p-like conduction band. The absence of parity symmetry in the YPtBi crystal structure generally causes further splitting of the bands away from the Γ-point. Because of the high symmetry of the cubic crystal structure of the half-Heusler material YPtBi, its MBJLDA electronic structure (see main text), shown in (**B**), retains the fourfold degeneracy of the p-like j = 3/2 states at the Γ-point. The solid and dashed horizontal lines represent μ determined by quantum oscillation and angle-ARPES experiments, respectively. (**C**) Theoretical spin-split Fermi surfaces obtained by fitting the j = 3/2 **k** · **p** theory in Eq. 1 to the ab initio results by fixing the chemical potential at μ = −35 meV (see main text).

requirement is only that the bands stem from a $j = 3/2$ representation at the Γ-point, and the nontrivial pairing states with nodes exist for all band structures as demonstrated in the study by Brydon *et al.* (*13*).

To determine the spin splitting of the true bulk Fermi surface, the angle-dependent Shubnikov–de Haas (SdH) effect was studied. First, we examine the magnetoresistance derivative, dR_{xx}/dB, to access directly to the oscillatory component. Figure 3A shows dR_{xx}/dB versus B at various in-plane angles ϕ defined from the crystallographic [010] direction, measured at $T = 2$ K. A node-like feature of beating oscillations, observable near 7 T for $\phi \le 10°$, moves in the magnetic field as the angle increases away from the highest symmetry direction. Angle-dependent SdH frequency (F), which is proportional to the cross-sectional area of Fermi surface maxima, was determined at the representative angles by using the fast Fourier transform (FFT) technique. The symmetrized plot of F versus ϕ is presented in Fig. 3B based on actual data with $0° \le \phi \le 90°$. At first glance, the SdH frequency is almost constant around $F = 46$ T (red line), which is consistent with a nearly spherical Fermi surface. Clear split peak was observed when $H \parallel [010]$, that is, $\phi = 0°$, with two frequencies of 39 and 50 T. The observed two frequencies correspond, respectively, to the inner and outer orbits of spin-split Fermi surfaces. To understand the nature of the Fermi surfaces associated with the two frequencies, we determined the temperature-dependent amplitude of the FFT spectra as shown in Fig. 3C. As temperature rises, the split-peak feature is no longer visible above $T = 10$ K due to thermal broadening of the corresponding Landau levels. A representative effective mass $m^* = 0.11 m_e$ by using the Lifshitz-Kosevich theory for both frequencies. The angle-dependent SdH data strongly support the theoretical spin-split Fermi surfaces.

To further constrain the pairing model, we focus on measurements of the temperature-dependent London penetration depth $\Delta\lambda(T)$, which is intimately related to the superconducting order parameter Δ (*27*). This approach is particularly useful in the case of YPtBi, where thermodynamic signatures of the superconducting state are difficult to measure, because λ^2 is inversely proportional to $N(0)$. The absolute value of the zero-temperature $\lambda(0)$ is 1.6 μm (*28*), about two orders of magnitude greater than that found in conventional superconductors with $T_c \sim 1$ K, such as zinc or aluminum.

As shown in Fig. 4A, a sharp and single superconducting transition at $T_c \approx 0.8$ K is observed, implying high quality of single crystal YPtBi. The transition temperature is consistent with transport measurements (*4*, *17*). We compare the low-temperature behavior of $\Delta\lambda(T)$ in YPtBi to that of KFe_2As_2 (*29*), an unconventional superconductor with line

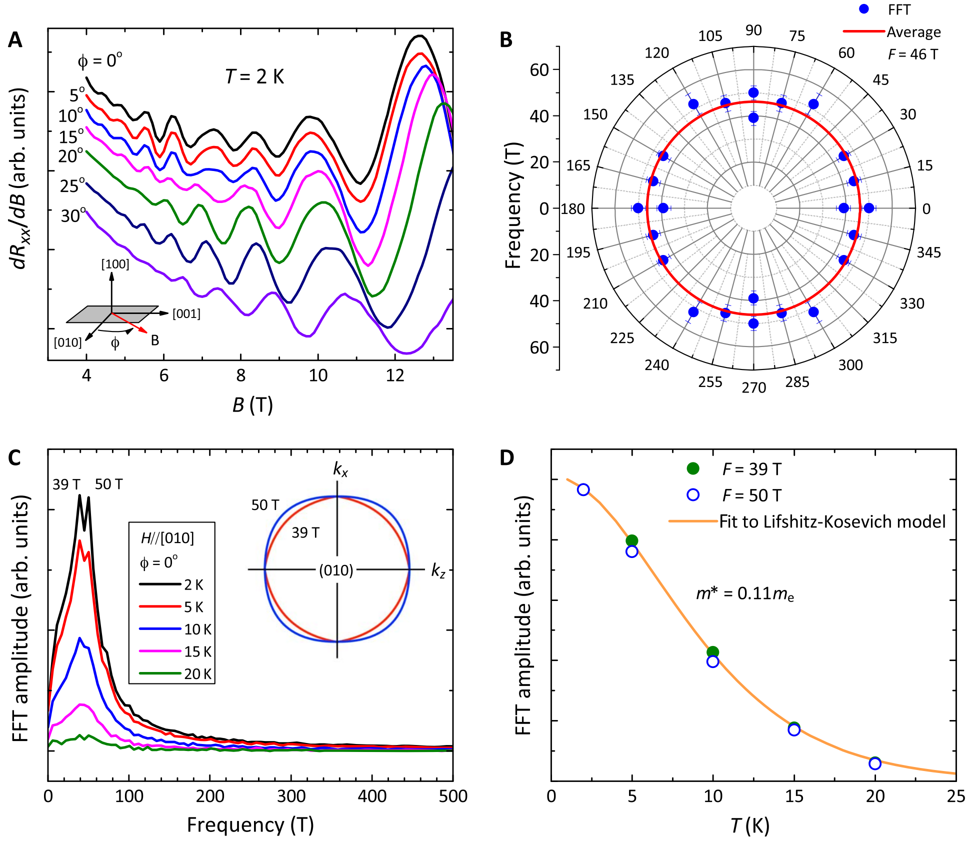

Fig. 3. Angle-dependent quantum oscillations in YPtBi. SdH oscillations were used to demonstrate the geometry of the spin-split Fermi surfaces. (**A**) dR_{xx}/dB versus B at $T = 2$ K is presented, measured at various in-plane angles ϕ defined from crystallographic [010] direction. A node of beating oscillation is observable near 7 T for $\phi \leq 10°$. The beating pattern changes as the angle is increased away from the high-symmetry direction. Actual magnetoresistance data R_{xx} are presented in the Supplementary Materials. (**B**) Angle-dependent frequency (F) was determined by using the FFT method on background subtracted oscillations (see the Supplementary Materials for details). The quantum oscillation frequency is nearly independent on the field orientation, and two frequencies are resolved when the field is applied with $\phi = 0°$, for example, $H \parallel [010]$. The red solid line is an averaged frequency, 46 T. The error bar is the frequency resolution of FFT. (**C**) Temperature-dependent FFT spectrum of SdH oscillations at $\phi = 0°$. The two frequencies, which are responsible for the beating pattern observed at $\phi \leq 10°$, are resolved to be 39 and 50 T, which correspond, respectively, to the inner and outer spin-split Fermi surfaces as shown in the inset. (**D**) The temperature-dependent amplitude of the FFT spectra is nearly identical for both spin-split Fermi surfaces as expected. A representative effective mass $m^* = 0.11m_e$ was determined by using the Lifshitz-Kosevich theory to both Fermi surfaces.

nodes (*29*), and the anisotropic *s*-wave superconductor $CaPd_2As_2$ (*30*), both taken using an identical experimental setup. The contrast is striking, with $\Delta\lambda(T)$ in YPtBi being nearly identical to that of KFe_2As_2 and completely different from that of $CaPd_2As_2$. In a fully gapped *s*-wave superconductor, the thermally activated quasi-particles are responsible for the expected exponential temperature dependence of $\Delta\lambda(T)$ at low temperatures (see the Supplementary Materials for details), whereas power laws are clear signatures of nodes or zeroes in the superconducting order parameter (*27*). In a gap structure with line nodes, the penetration depth varies linearly with temperature at sufficiently low temperatures ($T < 0.3T_c$) in a clean sample (see the Supplementary Materials for details) (*31*), as observed in the prototypical *d*-wave superconductor $YBa_2Cu_3O_{6.95}$ (YBCO) (*32*) and in the mixed-parity noncentrosymmetric superconductors CePt$_3$Si (*33*) and Li_2Pt_3B (*34*).

In YPtBi, we obtained the best least squares fitting for $\Delta\lambda(T)$ to a power-law function $\Delta\lambda = AT^n$ was obtained with $n = 1.20 \pm 0.02$ and $A = 1.98 \pm 0.08$ μm/K$^{1.2}$ in a temperature range that spans above $0.2T_c$. This nearly T-linear behavior is consistent with the expectation for a line-nodal superconductor. The observed small deviation from linearity is likely due to moderate impurity scattering, quantified by modifying the temperature dependence $\Delta\lambda(T) = bT^2/(T + T^*)$ (*35*) with scattering rate parameter $T^* = 0.07T_c$, indicating an exceptionally clean sample. The extraordinarily large power-law prefactor A in YPtBi is consistent with the London theory expectation $\lambda(0) \propto n^{-2}$ given the small carrier density of this material.

DISCUSSION

Line nodes could, in principle, arise from a large number of different pairing states. However, the cubic symmetry of YPtBi imposes severe constraints on the pairing: For example, the pure *d*-wave state realized in YBCO is very unlikely here, because it would be difficult to avoid mixing with another degenerate *d*-wave state. Although symmetry permits line nodes due to an extended *s*-wave state, this requires significant fine-tuning due to the small, nearly spherical Fermi surface of the material. Generic models for a nodal order parameter in YPtBi are concerned in a mixture of even-odd parity states, for example, singlet-triplet mixture. For T_d symmetry, the lowest orbital angular momentum A_1 triplet state is *f*-wave, which for small k gives gap functions on the two spin-split $j = 1/2$ Fermi surfaces (*13*). This state exhibits line nodes if the *f*-wave triplet gap Δ_f is larger than the *s*-wave singlet gap Δ_s. However, dominant *f*-wave symmetry of the Cooper pairs is highly unlikely if quasi-local interactions

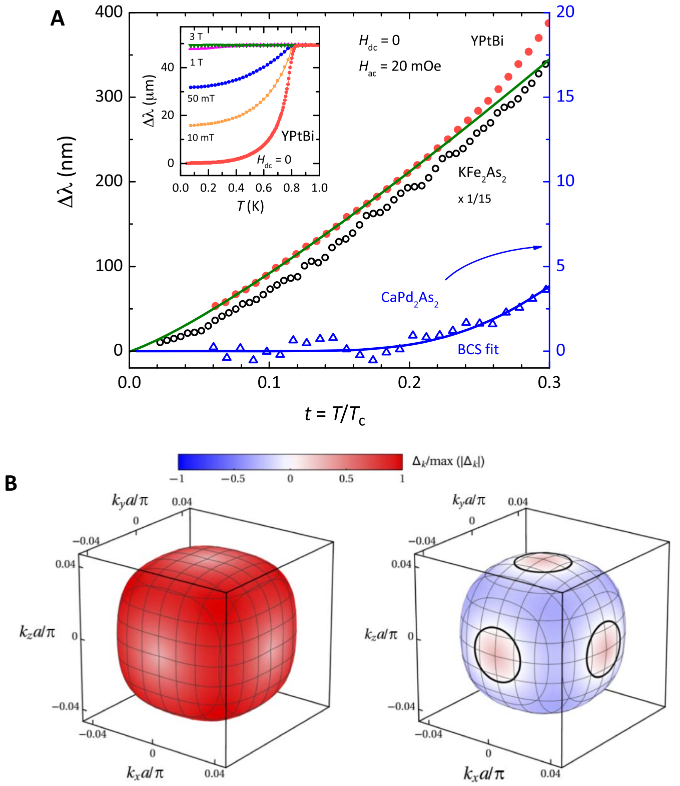

Fig. 4. Evidence for line nodes and spin-3/2 singlet-septet mixed parity pairing model. (**A**) The London penetration depth Δλ(*T*) of YPtBi (solid circles) measured in zero dc field (20 mOe ac field) is compared in (A) with that of KFe$_2$As$_2$ (open circles; T_c = 3.4 K), an unconventional superconductor with line nodes (*29*), and the anisotropic *s*-wave superconductor CaPd$_2$As$_2$ (open triangles; T_c = 1.3 K) (*30*), both taken by using an identical experimental setup. The nearly linear variation of Δλ(*T*) is in contrast with the full-gap BCS superconductor CaPd$_2$As$_2$ data (blue line), constraining any possible pairing model to one that yields line nodes. Inset shows Δλ in YPtBi under finite magnetic fields. Because of the high intrinsic angular momentum of the Γ_8 band quasiparticles involved in Cooper pairing in YPtBi, our *j* = 3/2 **k** · **p** model yields a manifold of possible pairing states with intrinsic angular momenta up to *J* = 3. Incorporating the lack of inversion symmetry, the singlet-septet pairing state is the simplest even-odd parity mixture with line nodes in the pairing gap that arise from the dominant *J* = 3 septet component (see main text). The gap sign and magnitudes are depicted in (**B**) for the two spin-dependent Fermi surfaces of YPtBi, showing the presence of line of zero-gap nodes (black lines) situated on one of the spin-dependent surfaces.

give rise to superconductivity (*36*); these interactions would more plausibly give rise to a *p*-wave state. The simplest and most generic scenarios for the nodal superconductivity in YPtBi are provided by a dominant *J* = 3 (septet) *p*-wave gap with a subdominant *J* = 0 (singlet) *s*-wave gap, as allowed by the noncentrosymmetric crystal structure.

As shown in Fig. 4B, the gap structure resulting from this mixed singlet-septet state displays ring-shaped line nodes on one of the spin-split Fermi surfaces. These line nodes are protected by a topological winding number and lead to nondegenerate surface zero-energy flat bands (see the Supplementary Materials for details) (*8*, *37*), which are of immense interest in the context of topological excitations. The mixed singlet-septet state is a natural generalization of the theory of *j* = 1/2 noncentrosymmetric superconductors. As discussed further in the Supplementary Materials however, the observation of gap line nodes and the broken inversion symmetry may be consistent with other exotic pairing states (*13*). Furthermore, with a conventional Eliashberg theory unapplicable to such a low-carrier density system, one must consider other pairing instabilities such as parity fluctuations (*38*) and instabilities due to apolar optical phonon (*39*) as possible mechanisms of superconductivity in the half-Heusler system. Studying the pairing mechanism of these exotic high–angular momentum pairing states, as well as their interplay with other symmetry-breaking orders (*5*), will elucidate the complexity and richness of this family of multifaceted topological materials.

METHODS

YPtBi single crystals were grown out of molten Bi with starting composition Y/Pt/Bi = 1:1:20 (atomic ratio). The starting materials Y ingot (99.5%), Pt powder (99.95%), and Bi chunk (99.999%) were put into an alumina crucible, and the crucible was sealed inside an evacuated quartz ampule. The ampule was heated slowly to 1150°C, kept for 10 hours, and then cooled down to 500°C at a 3°C/hour rate, where the excess of molten Bi was decanted by centrifugation.

The calculated band structure of YPtBi was obtained using the WIEN2k implementation of the full potential linearized augmented plane-wave method with the Tran-Blaha modified Becke-Johnson exchange-correlation potential (MBJLDA) (*40*), with SOC included in the calculation. The *k*-point mesh was taken to be 11× 11 ×11, and cubic lattice constant *a* = 664.0(1) pm was obtained from the study by Haase *et al.* (*26*).

The temperature variation of London penetration depth Δλ(*T*) was measured in a commercial dilution refrigerator by using a tunnel diode resonator technique. The single-crystal sample with dimensions 0.29 mm × 0.69 mm × 0.24 mm was mounted on a sapphire rod and inserted into a 2-mm inner diameter copper coil that produces radio frequency excitation field with empty-resonator frequency of 22 MHz with amplitude $H_{ac} \approx 20$ mOe. The shift of the resonant frequency (in centimeter gram second units) is $\Delta f(T) = -G4\pi\chi(T)$, where $\chi(T)$ is the differential magnetic susceptibility, $G = f_0V_s/2V_c(1-N)$ is a constant, *N* is the demagnetization factor, V_s is the sample volume, and V_c is the coil volume. The constant *G* was determined from the full frequency change by physically pulling the sample out of the coil. With the characteristic sample size, *R*, $4\pi\chi = (\lambda/R)\tanh(R/\lambda) - 1$, from which Δλ can be obtained (*27*).

Magnetic field–dependent magnetoresistance was determined on samples by using a standard four-probe technique. Contacts were made by using high-purity silver wires and conducting epoxy, and measurements were performed in a commercial cryostat with a single-axis rotator in magnetic fields up to 14 T at temperatures as low as 2 K.

SUPPLEMENTARY MATERIALS

Supplementary material for this article is available at http://advances.sciencemag.org/cgi/content/full/4/4/eaao4513/DC1

fig. S1. Band structre of YPtBi

fig. S2. Photon-dependent ARPES of Bi-terminated YPtBi(111).

fig. S3. Normalized magnitude of each gap along high symmetry points.

fig. S4. Superfluid density in YPtBi and other well-known superconductors.

fig. S5. Angle-dependent magnetoresistance in YPtBi.

fig. S6. Angle-dependent frequency of Shubnikov–de Haas quantum oscillation in YPtBi.

fig. S7. Temperature-dependent quantum oscillations with θ = 90° and ϕ = 0°.

REFERENCES AND NOTES

1. S. Chadov, X. Qi, J. Kübler, G. H. Fecher, C. Felser, S. C. Zhang, Tunable multifunctional topological insulators in ternary Heusler compounds. *Nat. Mater.* **9**, 541–545 (2010).

2. H. Lin, L. A. Wray, Y. Xia, S. Xu, S. Jia, R. J. Cava, A. Bansil, M. Z. Hasan, Half-Heusler ternary compounds as new multifunctional experimental platforms for topological quantum phenomena. *Nat. Mater.* **9**, 546–549 (2010).
3. D. Xiao, Y. Yao, W. Feng, J. Wen, W. Zhu, X.-Q. Chen, G. M. Stocks, Z. Zhang, Half-heusler compounds as a new class of three-dimensional topological insulators. *Phys. Rev. Lett.* **105**, 096404 (2010).
4. N. P. Butch, P. Syers, K. Kirshenbaum, A. P. Hope, J. Paglione, Superconductivity in the topological semimetal YPtBi. *Phys. Rev. B* **84**, 220504 (2011).
5. Y. Nakajima, R. Hu, K. Kirshenbaum, A. Hughes, P. Syers, X. Wang, K. Wang, R. Wang, S. R. Saha, D. Pratt, J. W. Lynn, J. Paglione, Topological RPdBi half-Heusler semimetals: A new family of noncentrosymmetric magnetic superconductors. *Sci. Adv.* **1**, e1500242 (2015).
6. R. S. K. Mong, A. M. Essin, J. E. Moore, Antiferromagnetic topological insulators. *Phys. Rev. B* **81**, 245209 (2010).
7. L. Fu, Odd-parity topological superconductor with nematic order: Application to $Cu_xBi_2Se_3$. *Phys. Rev. B* **90**, 100509 (2014).
8. A. P. Schnyder P. M. R. Brydon, Topological surface states in nodal superconductors. *J. Phys. Condens. Matter* **27**, 243201 (2015).
9. P. A. Frigeri, D. F. Agterberg, A. Koga, M. Sigrist, Superconductivity without inversion symmetry: MnSi versus $CePt_3Si$. *Phys. Rev. Lett.* **92**, 097001 (2004).
10. T.-L. Ho S. Yip, Pairing of fermions with arbitrary spin. *Phys. Rev. Lett.* **82**, 247–250 (1999).
11. C. Wu, J. Hu, S.-C. Zhang, Quintet pairing and non-abelian vortex string in spin-3/2 cold atomic systems. *Int. J. Mod. Phys. B.* **24**, 311 (2010).
12. W. Yang, Y. Li, C. Wu, Topological septet pairing with spin-$\frac{3}{2}$ fermions: High-partial-wave channel counterpart of the ^{3}He–B phase. *Phys. Rev. Lett.* **117**, 075301 (2016).
13. P. M. R. Brydon, L. Wang, M. Weinert, D. F. Agterberg, Pairing of $j = 3/2$ fermions in half-Heusler superconductors. *Phys. Rev. Lett.* **116**, 177001 (2016).
14. P. G. Pagliuso, C. Rettori, M. E. Torelli, G. B. Martins, Z. Fisk, J. L. Sarrao, M. F. Hundley, S. B. Oseroff, Crystal-field study in rare-earth-doped semiconducting YBiPt. *Phys. Rev. B* **60**, 4176–4180 (1999).
15. X. Lin, Z. Zhu, B. Fauqué, K. Behnia, Fermi surface of the most dilute superconductor. *Phys. Rev. X* **3**, 021002 (2013).
16. M. Meinert, Unconventional superconductivity in YPtBi and related topological semimetals. *Phys. Rev. Lett.* **116**, 137001 (2016).
17. T. V. Bay, T. Naka, Y. K. Huang, A. de Visser, Superconductivity in noncentrosymmetric YPtBi under pressure. *Phys. Rev. B* **86**, 064515 (2012).
18. T. V. Bay, T. Naka, Y. K. Huang, H. Luigjes, M. S. Golden, A. de Visser, Superconductivity in the doped topological insulator $Cu_xBi_2Se_3$ under high pressure. *Phys. Rev. Lett.* **108**, 057001 (2012).
19. K. Kirshenbaum, P. S. Syers, A. P. Hope, N. P. Butch, J. R. Jeffries, S. T. Weir, J. J. Hamlin, M. B. Maple, Y. K. Vohra, J. Paglione, Pressure-induced unconventional superconducting phase in the topological insulator Bi_2Se_3. *Phys. Rev. Lett.* **111**, 087001 (2013).
20. C. Shi, X. Xi, Z. Hou, X. Zhang, G. Xu, E. Liu, W. Wang, W. Wang, J. Chen, G. Wu, NMR investigation of atomic and electronic structures of half-Heusler topologically nontrivial semimetals. *Phys. Status Solidi B* **252**, 357–360 (2015).
21. W. Feng, D. Xiao, Y. Zhang, Y. Yao, Half-Heusler topological insulators: A first-principles study with the Tran-Blaha modified Becke-Johnson density functional. *Phys. Rev. B* **82**, 235121 (2010).
22. V. P. Mineev, K. V. Samokhin, de Haas–van Alphen effect in metals without an inversion center. *Phys. Rev. B* **72**, 212504 (2005).
23. C. Liu, Y. Lee, T. Kondo, E. D. Mun, M. Caudle, B. N. Harmon, S. L. Bud'ko, P. C. Canfield, A. Kaminski, Metallic surface electronic state in half-Heusler compounds *R*PtBi (*R* = Lu, Dy, Gd). *Phys. Rev. B* **83**, 205133 (2011).
24. Z. K. Liu, L. X. Yang, S.-C. Wu, C. Shekhar, J. Jiang, H. F. Yang, Y. Zhang, S.-K. Mo, Z. Hussain, B. Yan, C. Felser, Y. L. Chen, Observation of unusual topological surface states in half-Heusler compounds LnPtBi (Ln=Lu, Y). *Nat. Commun.* **7**, 12924 (2016).
25. G. Dresselhaus, Spin-orbit coupling effects in zinc blende structures. *Phys. Rev.* **100**, 580–586 (1955).
26. M. G. Haase, T. Schmidt, C. G. Richter, H. Block, W. Jeitschko, Equiatomic rare earth (*Ln*) transition metal antimonides *LnT*Sb (*T*=Rh, Ir) and Bismuthides *LnT*Bi (*T*=Rh, Ni, Pd, Pt). *J. Solid State Chem.* **168**, 18–27 (2002).
27. R. Prozorov, V. G. Kogan, London penetration depth in iron-based superconductors. *Rep. Prog. Phys.* **74**, 124505 (2011).
28. T. V. Bay, M. Jackson, C. Paulsen, C. Baines, A. Amato, T. Orvis, M. C. Aronson, Y. K. Huang, A. de Visser, Low field magnetic response of the non-centrosymmetric superconductor YPtBi. *Solid State Commun.* **183**, 13–17 (2014).
29. H. Kim, M. A. Tanatar, Y. Liu, Z. C. Sims, C. Zhang, P. Dai, T. A. Lograsso, R. Prozorov, Evolution of London penetration depth with scattering in single crystals of $K_{1-x}Na_xFe_2As_2$. *Phys. Rev. B* **89**, 174519 (2014).
30. V. K. Anand, H. Kim, M. A. Tanatar, R. Prozorov, D. C. Johnston, Superconducting and normal-state properties of APd_2As_2 (A = Ca, Sr, Ba) single crystals. *Phys. Rev. B* **87**, 224510 (2013).
31. D. Xu, S. K. Yip, J. A. Sauls, Nonlinear Meissner effect in unconventional superconductors. *Phys. Rev. B* **51**, 16233 (1995).
32. W. N. Hardy, D. A. Bonn, D. C. Morgan, R. Liang, K. Zhang, Precision measurements of the temperature dependence of λ in $YBa_2Cu_3O_{6.95}$: Strong evidence for nodes in the gap function. *Phys. Rev. Lett.* **70**, 3999–4002 (1993).
33. I. Bonalde, W. Brämer-Escamilla, E. Bauer, *Phys. Rev. Lett.* Evidence for line nodes in the superconducting energy gap of noncentrosymmetric $CePt_3Si$ from magnetic penetration depth measurements. *Phys. Rev. Lett.* **94**, 207002 (2005).
34. H. Q. Yuan, D. F. Agterberg, N. Hayashi, P. Badica, D. Vandervelde, K. Togano, M. Sigrist, M. B. Salamon, *S*-wave spin-triplet order in superconductors without inversion symmetry: Li_2Pd_3B and Li_2Pt_3B. *Phys. Rev. Lett.* **97**, 017006 (2006).
35. P. J. Hirschfeld, N. Goldenfeld, Effect of strong scattering on the low-temperature penetration depth of a *d*-wave superconductor. *Phys. Rev. B* **48**, 4219–4222 (1993).
36. R. Konno, K. Ueda, Superconductivity and antiferromagnetism in heavy-electron systems. *Phys. Rev. B* **40**, 4329 (1989).
37. S. Kobayashi, Y. Tanaka, M. Sato, Fragile surface zero-energy flat bands in three-dimensional chiral superconductors. *Phys. Rev. B* **92**, 214514 (2015).
38. V. Kozii, L. Fu, Odd-parity superconductivity in the vicinity of inversion symmetry breaking in spin-orbit-coupled systems. *Phys. Rev. Lett.* **115**, 207002 (2015).
39. L. Savary, J. Ruhman, J. W. F. Venderbos, L. Fu, P. A. Lee, Superconductivity in three-dimensional spin-orbit coupled semimetals. *Phys. Rev. B* **96**, 214514 (2017).
40. F. Tran, P. Blaha, Accurate band gaps of semiconductors and insulators with a semilocal exchange-correlation potential. *Phys. Rev. Lett.* **102**, 226401 (2009).

Acknowledgments: We acknowledge V. Yakovenko and M. Weinert for the stimulating discussion and S. Adams for her illustration works. **Funding:** Research at the University of Maryland was supported by the Department of Energy (DOE) Early Career Award No. DE-SC-0010605 (experimental investigations) and the Gordon and Betty Moore Foundation's EPiQS Initiative through grant no. GBMF4419 (materials synthesis). Work in Ames was supported by the U.S. DOE Office of Science, Basic Energy Sciences, Materials Science and Engineering Division. Ames Laboratory is operated for the U.S. DOE by the Iowa State University under contract no. DE-AC02-07CH11358. We acknowledge support from Microsoft Station Q, Laboratory for Physical Sciences–Condensed Matter Theory Center (LPS-CMTC), and Joint Quantum Institute–NSF–Physics Frontier Center (JQI-NSF-PFC) (P.M.R.B), and the NSF via DMREF-1335215 (D.F.A.). ARPES experiments were supported by the U.S. DOE at the Advanced Light Source (DE-AC02-05CH11231). **Author contributions:** K.W., S.Z., Y.N., and R.H. synthesized and characterized the crystals; H.K., M.A.T., and R.P. performed the penetration depth study; H.K., H.H., and P.S. performed the quantum oscillation study; P.M.R.B., L.W., and D.F.A. performed the DFT calculations and theoretical work; J.D.D. performed the ARPES study; and H.K., P.M.R.B., D.F.A., J.D.D., and J.P. wrote the manuscript. All the authors contributed to the discussion and interpretation of the experimental data. **Competing interests:** All authors declare that they have no competing interests. **Data and materials availability:** All data needed to evaluate the conclusions in the paper are present in the paper and/or the Supplementary Materials. Additional data related to this paper may be requested from the authors.

Submitted 24 July 2017
Accepted 15 February 2018
Published 6 April 2018
10.1126/sciadv.aao4513

Citation: H. Kim, K. Wang, Y. Nakajima, R. Hu, S. Ziemak, P. Syers, L. Wang, H. Hodovanets, J. D. Denlinger, P. M. R. Brydon, D. F. Agterberg, M. A. Tanatar, R. Prozorov, J. Paglione, Beyond triplet: Unconventional superconductivity in a spin-3/2 topological semimetal. *Sci. Adv.* **4**, eaao4513 (2018).

Science Advances

Beyond triplet: Unconventional superconductivity in a spin-3/2 topological semimetal

Hyunsoo Kim, Kefeng Wang, Yasuyuki Nakajima, Rongwei Hu, Steven Ziemak, Paul Syers, Limin Wang, Halyna Hodovanets, Jonathan D. Denlinger, Philip M. R. Brydon, Daniel F. Agterberg, Makariy A. Tanatar, Ruslan Prozorov and Johnpierre Paglione

Sci Adv **4** (4), eaao4513.
DOI: 10.1126/sciadv.aao4513

Science Advances

AAAS

advances.sciencemag.org/cgi/content/full/4/4/eaao4513/DC1

Supplementary Materials for

Beyond triplet: Unconventional superconductivity in a spin-3/2 topological semimetal

Hyunsoo Kim, Kefeng Wang, Yasuyuki Nakajima, Rongwei Hu, Steven Ziemak, Paul Syers, Limin Wang,
Halyna Hodovanets, Jonathan D. Denlinger, Philip M. R. Brydon, Daniel F. Agterberg,
Makariy A. Tanatar, Ruslan Prozorov, Johnpierre Paglione

Published 6 April 2018, *Sci. Adv.* **4**, eaao4513 (2018)
DOI: 10.1126/sciadv.aao4513

This PDF file includes:

- fig. S1. Band structre of YPtBi.
- fig. S2. Photon-dependent ARPES of Bi-terminated YPtBi(111).
- fig. S3. Normalized magnitude of each gap along high symmetry points.
- fig. S4. Superfluid density in YPtBi and other well-known superconductors.
- fig. S5. Angle-dependent magnetoresistance in YPtBi.
- fig. S6. Angle-dependent frequency of Shubnikov–de Haas quantum oscillation in YPtBi.
- fig. S7. Temperature-dependent quantum oscillations with θ = 90° and ϕ = 0°.

SPIN-3/2 PAIRING

In YPtBi, the electronic Γ_8 representation responsible for the states near the chemical potential can be described by a $j = 3/2$ basis with four basis elements: $\{|\frac{3}{2}\rangle, |\frac{1}{2}\rangle, |-\frac{1}{2}\rangle, |-\frac{3}{2}\rangle\}$. Physically this basis stems from $l = 1$ p-states coupled to $s = 1/2$ spin. In this direct product space, the basis elements can be expressed as

$$|\tfrac{3}{2}\rangle = \frac{1}{\sqrt{2}}[-|p_x, \tfrac{1}{2}\rangle - i|p_y, \tfrac{1}{2}\rangle] \tag{S1}$$

$$|\tfrac{1}{2}\rangle = \frac{1}{\sqrt{6}}[2|p_z, \tfrac{1}{2}\rangle - |p_x, -\tfrac{1}{2}\rangle - i|p_y, -\tfrac{1}{2}\rangle] \tag{S2}$$

$$|-\tfrac{1}{2}\rangle = \frac{1}{\sqrt{6}}[2|p_z, -\tfrac{1}{2}\rangle + |p_x, \tfrac{1}{2}\rangle - i|p_y, \tfrac{1}{2}\rangle] \tag{S3}$$

$$|-\tfrac{3}{2}\rangle = \frac{1}{\sqrt{2}}[|p_x, -\tfrac{1}{2}\rangle - i|p_y, -\tfrac{1}{2}\rangle] \tag{S4}$$

Cooper pairs can be constructed from these Γ_8 states. In particular using the angular momentum addition rule: $\frac{3}{2} \otimes \frac{3}{2} = 3 \oplus 2 \oplus 1 \oplus 0$, we can classify the sixteen possible Cooper pairs as follows

$J = 0$ singlet state

$$|J = 0, m_J = 0\rangle = \frac{1}{2}\Big(|\tfrac{3}{2}, -\tfrac{3}{2}\rangle - |-\tfrac{3}{2}, \tfrac{3}{2}\rangle - |\tfrac{1}{2}, -\tfrac{1}{2}\rangle + |-\tfrac{1}{2}, \tfrac{1}{2}\rangle\Big) \tag{S5}$$

$J = 1$ triplet states

$$\begin{aligned}
|J = 1, m_J = 1\rangle &= \frac{1}{\sqrt{10}}\Big(\sqrt{3}|\tfrac{3}{2}, -\tfrac{1}{2}\rangle - 2|\tfrac{1}{2}, \tfrac{1}{2}\rangle + \sqrt{3}|-\tfrac{1}{2}, \tfrac{3}{2}\rangle\Big) \\
|J = 1, m_J = 0\rangle &= \frac{1}{\sqrt{20}}\Big(3|\tfrac{3}{2}, -\tfrac{3}{2}\rangle - |\tfrac{1}{2}, -\tfrac{1}{2}\rangle - |-\tfrac{1}{2}, \tfrac{1}{2}\rangle + 3|-\tfrac{3}{2}, \tfrac{3}{2}\rangle\Big) \\
|J = 1, m_J = -1\rangle &= \frac{1}{\sqrt{10}}\Big(\sqrt{3}|-\tfrac{3}{2}, \tfrac{1}{2}\rangle - 2|-\tfrac{1}{2}, -\tfrac{1}{2}\rangle + \sqrt{3}|\tfrac{1}{2}, -\tfrac{3}{2}\rangle\Big)
\end{aligned} \tag{S6}$$

$J = 2$ quintet states

$$\begin{aligned}
|J = 2, m_J = 2\rangle &= \frac{1}{\sqrt{2}}\Big(|\tfrac{3}{2}, \tfrac{1}{2}\rangle - |\tfrac{1}{2}, \tfrac{3}{2}\rangle\Big) \\
|J = 2, m_J = 1\rangle &= \frac{1}{\sqrt{2}}\Big(|\tfrac{3}{2}, -\tfrac{1}{2}\rangle - |-\tfrac{1}{2}, \tfrac{3}{2}\rangle\Big) \\
|J = 2, m_J = 0\rangle &= \frac{1}{2}\Big(|\tfrac{3}{2}, -\tfrac{3}{2}\rangle + |\tfrac{1}{2}, -\tfrac{1}{2}\rangle - |\tfrac{1}{2}, -\tfrac{1}{2}\rangle - |-\tfrac{3}{2}, \tfrac{3}{2}\rangle\Big) \\
|J = 2, m_J = -1\rangle &= \frac{1}{\sqrt{2}}\Big(|-\tfrac{3}{2}, \tfrac{1}{2}\rangle - |\tfrac{1}{2}, -\tfrac{3}{2}\rangle\Big) \\
|J = 2, m_J = -2\rangle &= \frac{1}{\sqrt{2}}\Big(|-\tfrac{3}{2}, -\tfrac{1}{2}\rangle - |-\tfrac{1}{2}, -\tfrac{3}{2}\rangle\Big)
\end{aligned} \tag{S7}$$

and $J=3$ septet states

$$\begin{aligned}
|J=3,m_J=3\rangle &= |\tfrac{3}{2},\tfrac{3}{2}\rangle\\
|J=3,m_J=2\rangle &= \tfrac{1}{\sqrt{2}}\Big(|\tfrac{3}{2},\tfrac{1}{2}\rangle+|\tfrac{1}{2},\tfrac{3}{2}\rangle\Big)\\
|J=3,m_J=1\rangle &= \tfrac{1}{\sqrt{5}}\Big(|\tfrac{3}{2},-\tfrac{1}{2}\rangle+\sqrt{3}|\tfrac{1}{2},\tfrac{1}{2}\rangle+|-\tfrac{1}{2},\tfrac{3}{2}\rangle\Big)\\
|J=3,m_J=0\rangle &= \tfrac{1}{\sqrt{20}}\Big(|\tfrac{3}{2},-\tfrac{3}{2}\rangle+3|\tfrac{1}{2},-\tfrac{1}{2}\rangle+3|-\tfrac{1}{2},\tfrac{1}{2}\rangle+|-\tfrac{3}{2},\tfrac{3}{2}\rangle\Big)\\
|J=3,m_J=-1\rangle &= \tfrac{1}{\sqrt{5}}\Big(|\tfrac{3}{2},-\tfrac{1}{2}\rangle+\sqrt{3}|-\tfrac{1}{2},-\tfrac{1}{2}\rangle+|\tfrac{1}{2},-\tfrac{3}{2}\rangle\Big)\\
|J=3,m_J=-2\rangle &= \tfrac{1}{\sqrt{2}}\Big(|-\tfrac{3}{2},-\tfrac{1}{2}\rangle+|-\tfrac{1}{2},-\tfrac{3}{2}\rangle\Big)\\
|J=3,m_J=-3\rangle &= |-\tfrac{3}{2},-\tfrac{3}{2}\rangle
\end{aligned}\tag{S8}$$

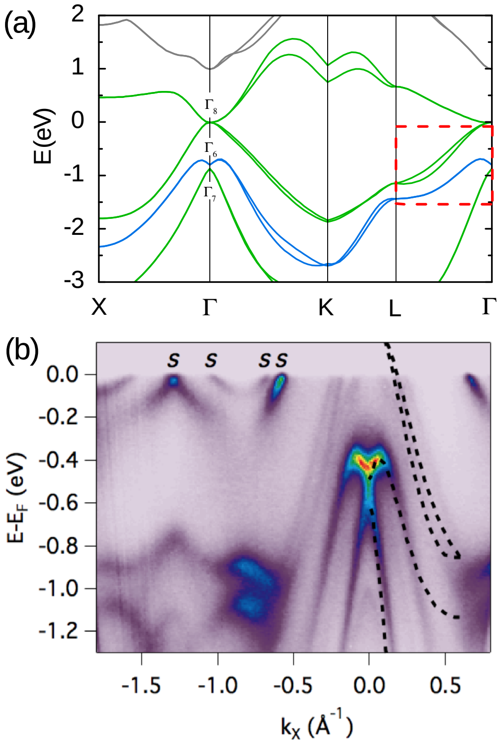

fig. S1. Comparison of YPtBi bulk band structure to ARPES. (a) Calculated band structure of YPtBi obtained using the full potential linearized augmented plane wave method with the Tran-Blaha modified Becke-Johnson exchange-correlation potential (MBJLDA). (b) Results of angle-dependent photoemission spectroscopy (ARPES) measurement done on Bi-terminated (111) surface. The black dashed lines represent the calculated band structure along Γ-L. The chemical potential in ARPES result is about 0.32 eV below that of theoretical result.

ELECTRONIC STRUCTURE

Figure S1 presents the band structure of YPtBi. The calculated band structure of YPtBi shown in panel (a) was obtained using the WIEN2k implementation of the full potential linearized augmented plane wave method with the Tran-Blaha modified Becke-Johnson exchange-correlation potential (MBJLDA) [40], with spin-orbital coupling included in the calculation. The k-point mesh was taken to be 11×11×11, and cubic lattice constant $a = 664.0(1)$ pm was obtained from elsewhere [26]. The s-like band Γ_6 lies below the p-like band Γ_8, reflecting the nontrivial topology, consistent with previous calculations [1-3]. Note the splittings will disappear in a non-relativistic calculation, and also it is common to have these spin splittings vanish at high symmetry points and along high symmetry directions. This is because there are symmetry elements that require band degeneracies, which are removed when we move away from these special points. This splitting evidences a j=3/2 analogue of anti-symmetric spin-orbit coupling (ASOC) due to broken inversion symmetry, similar to Rashba spin-orbit coupling in tetragonal systems [25].

Figure S1(b) shows an ARPES high symmetry valence band dispersion image at $h\nu = 86$ eV for the Bi-terminated (111) surfaces of YPtBi, acquired at beamline 4.0.3 of the Advanced Light Source at $T = 30$ K. Numerous bands are observed to cross the Fermi-level (E_F) from the zone boundary to normal emission. Consistent with ARPES measurements of LuPtBi and GdPtBi [23], the photon energy dependence of most of these bands follows strong vertical streaks along k_z indicative of 2D surface states. Theoretical slab calculations [23] have determined that the surface states, labeled s in fig. S1(b), originate from a Bi-terminated (111) cleavage plane, and that they are of non-topological origin owing to an even number of E_F-crossings with the surface Brillouin zone. Aging of the surface in a poorer storage vacuum for a week is observed to suppress all the surface states and leave a single fuzzy broad hole-band feature that reaches to E_F. A similar inner-hole band pocket was also observed as a single-band with weak intensity in LuPtBi and GdPtBi [23] and assumed to be a pair of nearly degenerate bands from comparison to their slab calculations.

A characteristic Rashba-like splitting of two hole bands is shown in fig. S1(b) at ≈ 0.5 eV binding energy which

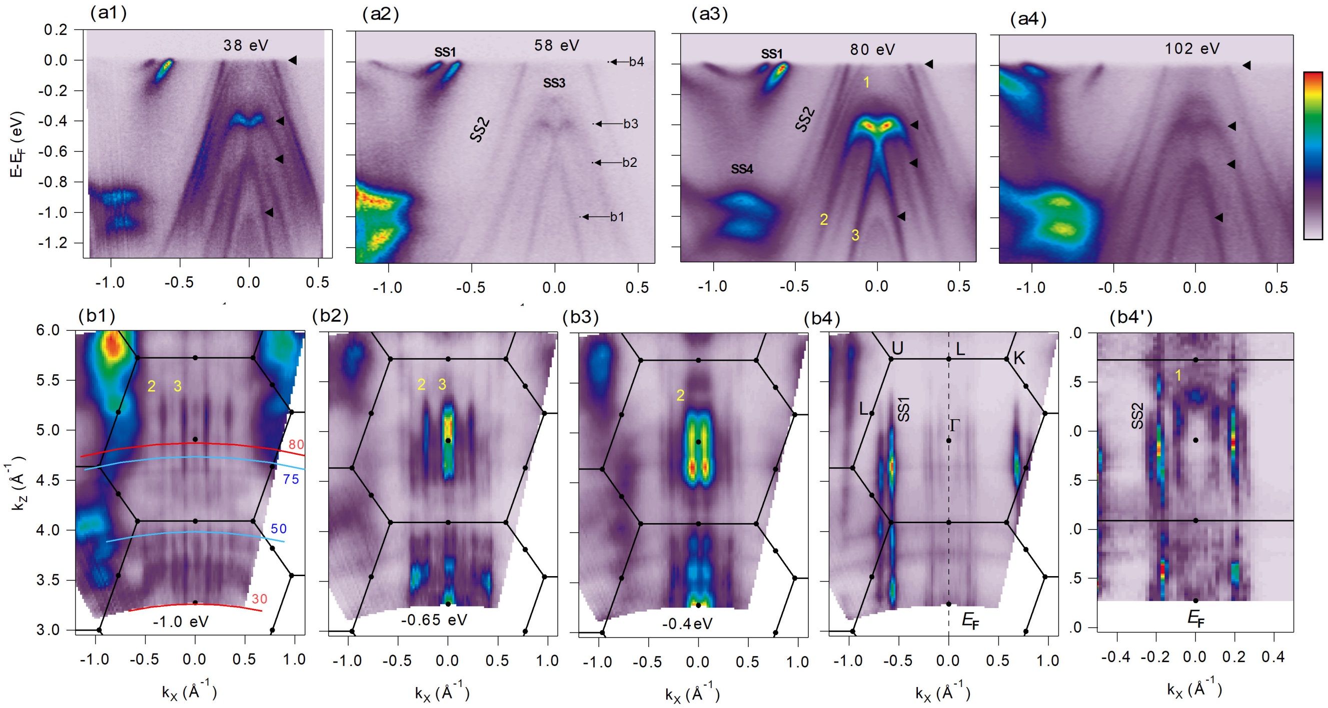

fig. S2. Photon dependence of Bi-terminated YPtBi(111). (a) Normal emission band dispersion images at select photon energies. (b) k_x-k_z intensity maps at select binding energies as marked by arrows in panel (a2) and with overplotted Brillouin zone boundaries with (111) along k_z. The ARPES data are converted to k_z using an inner potential parameter of 15 eV. Red (blue) arcs in panel (b1) indicate the photon energy ranges probed by Ref. [23] (30-80 eV) and by Ref. [24] (50-75 eV). Bi-termination surfaces states (SS1-SS4) and other bulk-derived states with band-bending-induced 2D character (1-3) are labeled in both (a) and (b).

also appear in bulk band structure calculations, but at an energy of ≈ -0.8 eV below E_F. Shifting the theory Γ-L bands to higher energy by ≈ 0.3 eV to align to the Rashba-like split bulk bands, as shown in overplotted dashed lines, causes two other nearly-degenerate hole-like bulk bands that originally just touch E_F at a semimetal point, to form a hole-pocket. This large 0.3 eV chemical potential shift in the ARPES measurement, relative to the theory calculation, reflects a possible charge imbalance at the cleaved surface and resultant band bending relative to the bulk.

In order to determine the bulk or surface character of the ARPES bands, we have performed photon energy dependence on Bi-terminated (111) surfaces of YPtBi. The photon dependent ARPES map cuts shown in fig. S2 reveal two different kinds of surface states: (i) surface-localized Bi-terminated dangling bond states and (ii) bulk-derived states that acquire 2D character from the p-type surface band bending that results from the Bi-termination charge balance and pinning of the chemical potential at the surface. The Bi surface states, SS1-SS4, exhibit vertical streaks along k_z in the constant binding energy intensity cuts, e.g. SS1 in (b4) and SS2 in (b4'), with a strong presence at all photon energies. This lack of k_z-variation with weak intensity variation uncorrelated to the bulk Brillouin zone (BZ) reflects a 2D origin from the top few layers of the surface, e.g. narrowly confined Δz causes extended Δk_z. Other states labeled (1-3) in fig. S2 exhibit a distinctly different intensity profile of finite segments of strong intensity along k_z centered on the bulk Γ-point, and with length < 1/2 the height of the overplotted (111)-oriented BZ boundaries. This finite k_z length of the strong photoemission intensity reflects a deeper depth origin ($\Delta z \approx 2\pi/\Delta k_z$) of these states. e.g. at least two (111) unit cells in real space.

This distinct intensity behavior as a function of photon energy was not previously revealed in ARPES studies with limited photon energy ranges of 30-80 eV in Ref. [23] and 50-75 eV in Ref. [24] as plotted in fig. S2 (b1). This behavior is consistent with bulk-derived quantum well states with a depth penetration that is determined by the z-profile of the band-bending potential. Furthermore, a finite gap between bands 2 and 3 at $k_x = 0$ is suggested by the dispersion images in panels (a1,a4) at 38 eV and 102 eV, consistent with the bulk theory band structure shown in fig. S1. The filling in of the gap and full Rashba-like appearance is then conjectured to arise from a topological surface state with Dirac crossing that connects between the bulk-like bands 2 and 3. This scenario is consistent with the theoretical calculations Ref. [24].

The experimental quantum oscillation frequency of $F \approx 45$ T [4] corresponds to a cross sectional area of a hypothetical spherical Fermi surface $A_F \approx 0.43$ nm^{-2} and a $k_{\mathrm{F}} {\approx} 0.037$ Å^{-1}, using the Onsager relation $F = \phi_0 A_F / 2\pi^2$ where $A_F = \pi k_F^2$ and $\phi_0 = 2.07 \times 10^{-7}$ G cm^{-2}, which is much smaller than the ARPES k_{F} values in fig. S1(b) of ≈ 0.1 Å^{-1}. This supports the scenario of a charge imbalance at the surface and band bending with the bulk chemical potential only ≈35 meV below the hole-band maximum. This justifies the vertical energy shift used to match to the calculated DFT band structure and quantum oscillations experiments.

$j = 3/2$ $\mathbf{k} \cdot \mathbf{p}$ MODEL

We treat the ASOC as a perturbation of the Luttinger-Kohn model, which has doubly-degenerate eigenenergies

$$\epsilon_{\mathbf{k},\pm} = \left(\alpha + \frac{5}{4}\beta\right) |\mathbf{k}|^2 \pm \beta \sqrt{\sum_i \left[k_i^4 + \left(\tfrac{3\gamma^2}{\beta^2} - 1\right) k_i^2 k_{i+1}^2\right]} \tag{S9}$$

Due to the presence of time-reversal and inversion symmetry for $\delta = 0$, the eigenstates can be labelled by a pseudospin-1/2 index. Proceeding via degenerate perturbation theory, we now include the ASOC by projecting it into the pseudospin basis for each band, hence obtaining two effective pseudospin-1/2 Hamiltonians

$$H_{\mathrm{eff},\pm} = \epsilon_{\mathbf{k},\pm} \hat{s}_0 + \mathbf{g}_{\mathbf{k},\pm} \cdot \hat{\mathbf{s}} \tag{S10}$$

where $\hat{s}_\mu$ are the Pauli matrices for the pseudospin, and the vector $\mathbf{g}_{\mathbf{k},\pm} = -\mathbf{g}_{-\mathbf{k},\pm}$ represents the effective ASOC in the pseudospin-1/2 basis of the band $\epsilon_{\mathbf{k},\pm}$. The expression for $\mathbf{g}_{\mathbf{k},\pm}$ is complicated and depends upon the choice of pseudospin basis; an analytic expression for $|\mathbf{g}_{\mathbf{k},\pm}|$ is given elsewhere [13]. The effective pseudospin-1/2 Hamiltonians can be diagonalized by going over to the helicity basis, yielding dispersions $E_{\mathbf{k},\eta=\pm,\nu=\pm} = \epsilon_{\mathbf{k},\eta} + \nu |\mathbf{g}_{\mathbf{k},\eta}|$, where the values of η and ν are independent of one another. In particular, the two spin-split Fermi surfaces are labelled by opposite values of ν. This approximation is in excellent agreement with the exact solutions of the $\mathbf{k} \cdot \mathbf{p}$ for small antisymmetric SOC.

In weak-coupling Bogoliubov-de Gennes theory the pairing is modelled by a term in the Hamiltonian of the form

$$H_{\mathrm{pair}} = \sum_{\mathbf{k}} \sum_{j,j'=-3/2}^{3/2} \left\{ \Delta_{j,j'}(\mathbf{k}) c_{\mathbf{k},j}^\dagger c_{-\mathbf{k},j'}^\dagger + \mathrm{H.c.} \right\} \tag{S11}$$

We restrict our attention to gaps in the A_1 irreducible representation of the T_d point group (i.e. with the full symmetry of the lattice). Allowing pairing in at most a relative p-wave (assuming quasi-local interactions are responsible for the superconductivity, higher-order momentum-dependence is unlikely [36]), we have the general gap

$$\check{\Delta}(\mathbf{k}) = \Delta_s \begin{pmatrix} 0 & 0 & 0 & 1 \\ 0 & 0 & -1 & 0 \\ 0 & 1 & 0 & 0 \\ -1 & 0 & 0 & 0 \end{pmatrix} + \Delta_p \begin{pmatrix} \frac{3}{4}k_- & \frac{\sqrt{3}}{2}k_z & \frac{\sqrt{3}}{4}k_+ & 0 \\ \frac{\sqrt{3}}{2}k_z & \frac{3}{4}k_+ & 0 & -\frac{\sqrt{3}}{4}k_- \\ \frac{\sqrt{3}}{4}k_+ & 0 & -\frac{3}{4}k_- & \frac{\sqrt{3}}{2}k_z \\ 0 & -\frac{\sqrt{3}}{4}k_- & \frac{\sqrt{3}}{2}k_z & -\frac{3}{4}k_+ \end{pmatrix} \tag{S12}$$

where $k_\pm = k_x \pm i k_y$. This constitutes a mixed state involving s-wave singlet pairing with strength Δ_s and p-wave *septet* pairing with strength Δ_p. The gap near the Fermi energy can be found by projecting Eq. (S12) into the effective pseudospin-1/2 bands, yielding

$$\Delta_{\mathrm{eff},\pm} = \left[\Delta_s + (\Delta_p/\delta)(\mathbf{g}_{\mathbf{k},\pm} \cdot \hat{\mathbf{s}})\right] i\hat{s}_y \tag{S13}$$

This describes a mixture of pseudodspin-singlet and pseudospin-triplet pairing. Importantly, the **d**-vector of the effective pseudospin-triplet pairing is parallel to the ASOC vector $\mathbf{g}_{\mathbf{k},\pm}$. As pointed out by Frigeri *et al.* [9], this alignment makes the pseudospin-triplet component immune to the pair-breaking effect of the ASOC; for sufficiently large ASOC, it is the only stable odd-parity gap. If the singlet state is subdominant, the resulting gap displays line nodes on one of the spin-split Fermi surfaces.

Although the nodal gap prevents us from defining a global topological invariant, the nodal lines themselves represent a nontrivial topological defect in the Brillouin zone. Specifically, the Bogoliubov-de Gennes Hamiltonian $H_{BdG}(\mathbf{k})$ belongs to Altland-Zirnbauer class DIII, which implies that it can be brought into off-diagonal form. This allows us to define the winding number

$$W_{\mathcal{L}} = \frac{1}{2\pi} \mathrm{Im} \oint_{\mathcal{L}} dl \mathrm{Tr} \left\{ \nabla_l \ln(D_{\mathbf{k}}) \right\} \tag{S14}$$

where $D_{\mathbf{k}}$ is the upper off-diagonal block of the Hamiltonian [8]. The winding number $W_{\mathcal{L}}$ takes an integer value along any closed path $\mathcal{L}$ in the Brillouin zone that does not intersect a gap node. Moreover, it is only nonzero if

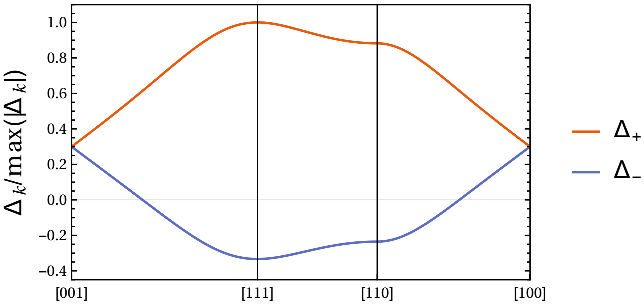

fig. S3. Normalized magnitude of each gap $\Delta_\mathbf{k}/\max(|\Delta_\mathbf{k}|)$ along high symmetry points is presented for full gap and nodal gap in red and blue, respectively. Whereas the fully gapped branch (red) contributes only thermally activated quasiparticles at low temperatures, the line-node branch (blue) manifests a linear temperature variation of the London penetration depth $\Delta\lambda \propto T$, consistent with experimental observations in YPtBi.

the path $\mathcal{L}$ encircles a line node, defining the topological charge of the node which in our case evaluates to ±1. This topological charge ensures the existence of a nondegenerate zero-energy surface flat band within the projection of the line node in the surface Brillouin zone [8].

Some alternatives to the mixed singlet-septet state proposed here should be noted. In particular, for purely local pairing interactions, there are five additional s-wave states with quintet total angular momentum [13]. Within a weak-coupling theory, these combine to give time-reversal symmetry-breaking states gaps with Weyl point nodes, and in some cases also line nodes. While such pairing states also topological, they do not yield robust zero-energy surface flat bands [37].

Figure S3 shows distribution of gap amplitudes $\Delta_k/\max(|\Delta_k|)$ along high symmetry points on the spin-split Fermi surfaces of YPtBi, with a full gap on the outer Fermi surface and gap with line nodes on the inner Fermi surface (see Fig. 4 in the main text for the gap structure on the entire Fermi surface). Whereas the fully gapped branch (Δ_+) contributes only thermally activated quasiparticles at low temperatures, the line-node branch (Δ_-) manifests a linear temperature variation of the London penetration depth $\Delta\lambda \propto T$, consistent with experimental observations in YPtBi.

LONDON PENETRATION DEPTH AND SUPERFLUID DENSITY

The temperature variation of London penetration depth is intimately related to the superconducting order parameter Δ. Within a weak coupling Eilenberger quasiclassical formulation with the perturbation theory

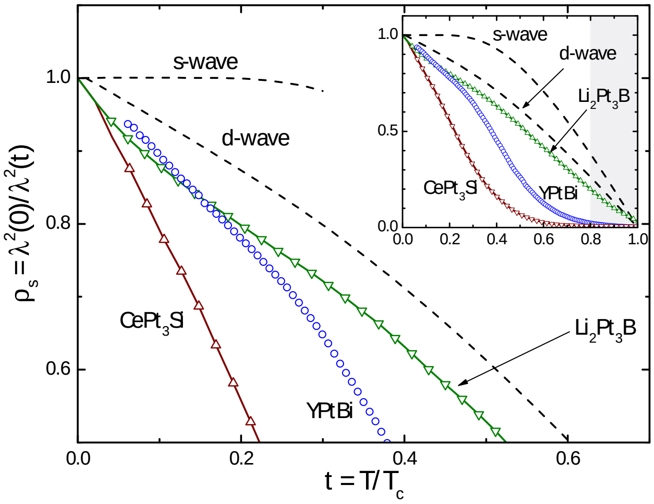

fig. S4. Superfluid density in YPtBi and other well-known superconductors. The normalized superfluid density was calculated by using a relation, $\rho_s = \lambda^2(0)/\lambda^2(T)$ where $\lambda(0) = 1.6\mu$m [30]. Theoretical singlet s-wave and d-wave are shown in dashed lines, and experimental data from noncentrosymmetric superconductors are shown in triangle symbols for CePt$_3$Si (Ref. [33]) and Li$_2$Pt$_3$B (Ref. [34]).

of a weak magnetic field [27]

$$(\lambda^2)^{-1}_{ik} = \frac{16\pi^2 e^2 T}{c^2} N(0) \sum_\omega \left\langle \frac{\Delta^2 v_i v_k}{(\Delta^2 + \hbar^2\omega^2)^{3/2}} \right\rangle \quad \text{(S15)}$$

where $N(0)$ is the total density of states at Fermi level per spin, v is the Fermi velocity, and ω is the Matsubara frequency. Measurement of the London penetration depth utilizes a small excitation field $H_{ac} < 20$ mOe, so the Eq. (S15) is valid in absence of H_{dc}.

In an s-wave superconductor, an exponential behavior of $\Delta\lambda(T)/\lambda(0) = \sqrt{\pi\Delta_0/2k_BT}\exp(-\Delta_0/k_BT)$ can be deduced from Eq. (S15) for a constant gap $\Delta = \Delta_0$, i.e., at low temperatures $T < T_c/3$, while in a d-wave superconductor $\Delta\lambda(T)$ varies linearly with temperature as $\Delta\lambda(T) = \frac{2\lambda(0)\ln 2}{\eta\Delta_0}T$, at sufficiently low temperatures in a clean sample [31]. Here, η is the angular slope parameter near the node, *e.g.,* $\eta = 2$ for a d-wave gap $\Delta = \Delta_0(k_x^2 - k_y^2)$. To compare the experimental result for YPtBi to the d-wave gap expectation, one can fix the temperature power of $\Delta\lambda(T)$ to $n = 1$ and obtain a slope prefactor $A = 1.5$ μm/K from fitting, yielding $2\Delta_0/k_BT_c \approx 4/\eta$. Fixing $\eta = 2$ for the d-wave case gives $2\Delta_0 \approx 2k_BT_c$, which is slightly smaller than the weak-coupling BCS value of $2\Delta_0 = 3.52k_BT_c$.

The normalized superfluid density in YPtBi is calculated by using a relation, $\rho_s = \lambda^2(0)/\lambda^2(T)$. Here we used $\lambda(0) = 1.6$ μm determined by μSR experiments [28]. The calculated ρ_s is compared to that of well-known superconductors in fig. S4. Theoretical ρ_s of singlet s-wave and d-wave superconductors are shown in dashed

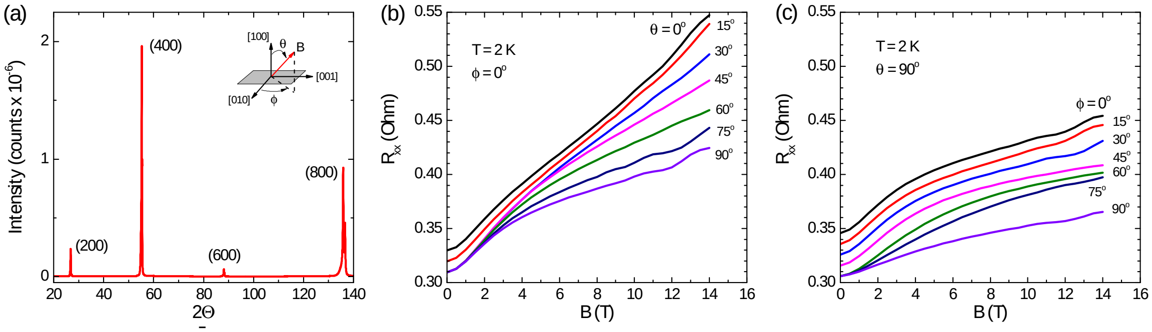

fig. S5. Angle-dependent magnetoresistance in YPtBi. (a) Single crystal x ray diffraction pattern of (100) surface of YPtBi used for angle-dependent quantum oscillation experiments. A schematic defines two controlled angles θ and ϕ. Angle-dependent magnetoresistance (b) with varying θ at fixed $\phi = 0°$ and (c) with varying ϕ at fixed $\theta = 90°$. Shubnikov-de Haas quantum oscillations are evident in most of the orientations.

lines, and the experimental ρ_s from two other noncentrosymmetric superconductors, CePt$_3$Si [33] and Li$_2$Pt$_3$B [34], are shown in triangle symbols. Whereas the singlet s-wave does not exhibit noticeable temperature-variation up to $0.2T_c$, the other nodal superconductors show nearly linear temperature-dependence. The superfluid density in CePt$_3$Si is most compatible with an order parameter with two vector components [33] and that in Li$_2$Pt$_3$B is consistent with a spin singlet-triplet mixed pairing with the triplet component being dominant [34]. Interestingly, the superfluid density in YPtBi has similar behavior to that of the other noncentrosymmetric superconductors, and is consistent with multigap, line-nodal superconducting order parameter.

We note that the value of penetration depth rapidly approaches the characteristic size of the sample R (see Methods for detail) near T_c because of large $\lambda(0)$ in YPtBi ($\Delta\lambda(T) \propto \lambda(0)$). In this temperature range, the measurement is in an extreme sample size-limiting effect, and the temperature-variation of both $\Delta\lambda$ and ρ_s in YPtBi are severely affected by this effect. Therefore, the superfluid density near T_c should not be taken seriously, and we highlighted the problematic region in the inset of fig. S4.

ANGLE-DEPENDENT MAGNETORESISTANCE

Angle-dependent magnetoresistance was measured to study the spin-split Fermi surface of YPtBi. A sample was cut out of (100) plane confirmed by a single-crystal diffraction pattern as shown in fig. S5(a). The angle-dependence of the longitudinal magnetoresistance R_{xx} was measured by using a single-axis rotator at various orientations with two controlled angles θ and ϕ defined in fig. S5(a). Panel (b) shows angle-dependent magnetoresistance data with varying θ from 0° to 90° at $\phi = 0°$. At most of the angles, Shubnikov-de Haas (SdH) quantum oscillations are visible on smoothly increasing magnetoresistance. Similar experiments with varying ϕ from 0° to 90° at $\theta = 90°$ were done and presented in fig. S5(c). In both configurations, SdH oscillations show angle-dependence where the amplitude and phase changes at different orientations of the applied magnetic field implying the SdH consists of multiple frequencies with varying frequencies and relative phases. The oscillations at 0° and 90° in both configurations appear the same, confirming the assignment of crystallographic orientation in the schematic.

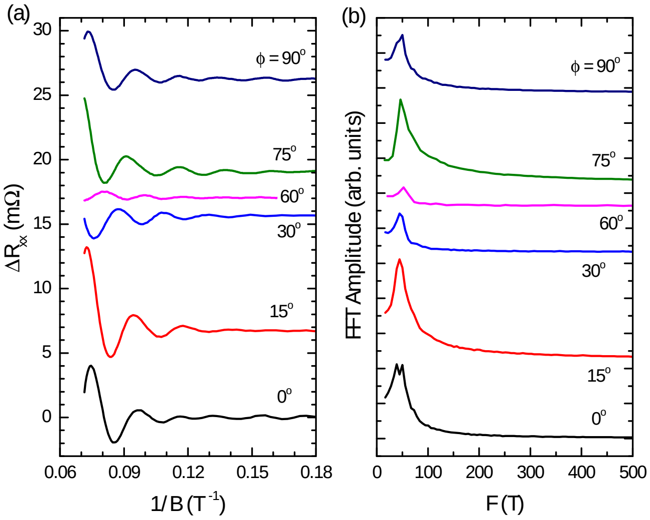

fig. S6. Angle-dependent frequency of Shubnikov-de Haas quantum oscillation in YPtBi. (a) SdH quantum oscillations extracted from the magnetoresistance at selected ϕ angles with fixed $\theta = 90°$. (b) Fast Fourier transform spectra obtained from the quantum oscillations shown in (a). The angles are defined in fig. S5.

Figure S6(a) shows the SdH quantum oscillations obtained from the magnetoresistance data in fig. S5(c). The angle-dependence of SdH oscillation is clear while the oscillations at $\phi = 0°$ and 90° oscillations are nearly identical in both of which display a beating node around $B^{-1} = 0.12$ T^{-1}. We employ the fast Fourier transform

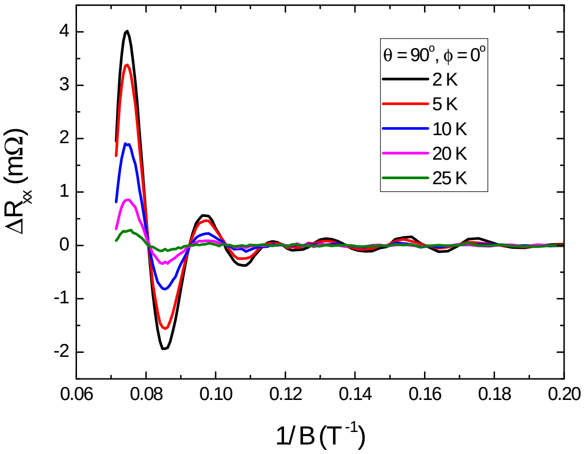

fig. S7. Temperature-dependent quantum oscillations with $\theta = 90^\circ$ and $\phi = 0^\circ$. The angles are defined in fig. S5.

(FFT) to determined the frequency for several elected angles. The FFT-spectra are shown in fig. S6(b). At first glance, the spectrum shows a broad peak around $F = 46$ T at all selected angles. The angular variation of the determined frequencies is presented in Fig. 3(b) in the main text. In some orientations, it shows a broad feature with double peaks, and the two peaks are clearly resolved in the data for $\phi = 0^\circ$ with two frequencies of 39 ± 3 T and 50 ± 3 T where the error bar is the frequency resolution of FFT. We attributed the observation of two frequencies to existence of spin-split Fermi surfaces. Using a theory by Mineev and Samokhin [22], the estimated energy of spin-orbit coupling is about 1 meV when Zeeman interaction is much smaller than spin-orbit interaction.

To learn the nature of the Fermi surfaces associated with two resolved frequencies, we measured temperature-dependent SdH quantum oscillations with field along [010], i.e., $\theta = 90^\circ$ and $\phi = 0^\circ$. Temperature dependent SdH oscillations are displayed in fig. S7, FFT-spectra of which are presented in Fig. 3(c) in the main text. We determined effective mass from temperature dependence of the amplitude by using the Lifshitz-Kosevich theory as shown in Fig. 3(d) in the main text. They have nearly identical effective mass as expected for spin-split Fermi surfaces.